

NuSTAR view of the central region of M 31

H. Stiele¹*, A. K. H. Kong^{1,2}

¹National Tsing Hua University, Department of Physics and Institute of Astronomy, No. 101 Sect. 2 Kuang-Fu Road, 30013, Hsinchu, Taiwan

²Astrophysics, Department of Physics, University of Oxford, Keble Road, Oxford OX1 3RH, UK

2018 January 16

ABSTRACT

Our neighbouring large spiral galaxy, the Andromeda galaxy (M 31 or NGC 224), is an ideal target to study the X-ray source population of a nearby galaxy. *NuSTAR* observed the central region of M 31 in 2015 and allows studying the population of X-ray point sources at energies higher than 10 keV. Based on the source catalogue of the large *XMM-Newton* survey of M 31, we identified counterparts to the *XMM-Newton* sources in the *NuSTAR* data. The *NuSTAR* data only contain sources of a brightness comparable (or even brighter) than the selected sources that have been detected in *XMM-Newton* data. We investigate hardness ratios, spectra and long-term light curves of individual sources obtained from *NuSTAR* data. Based on our spectral studies we suggest four sources as possible X-ray binary candidates. The long-term light curves of seven sources that have been observed more than once show low (but significant) variability.

Key words: galaxies: individual: M 31 X-rays: galaxies – X-rays: binaries

1 INTRODUCTION

With a distance of 780 kpc (Holland 1998; Stanek & Garnavich 1998) and moderate Galactic foreground absorption ($N_{\mathrm{H}}=7\times10^{20}$ cm⁻² Stark et al. 1992), the Andromeda galaxy (M 31 or NGC 224), is an ideal target to study the X-ray source population of a neighbouring large spiral galaxy. M 31 has been observed with many different X-ray imaging satellites, including *Einstein* (van Speybroeck et al. 1979; Collura et al. 1990; Trinchieri & Fabbiano 1991), *ROSAT* (Primini et al. 1993; Supper et al. 1997, 2001), *Chandra* (Garcia et al. 2000; Di Stefano et al. 2002; Kaaret 2002; Kong et al. 2002; Di Stefano et al. 2004; Williams et al. 2004; Voss & Gilfanov 2007; Hofmann et al. 2013), *Swift* (Voss et al. 2008), and *XMM-Newton* (Osborne et al. 2001; Orio et al. 2010; Pietsch et al. 2005, 2007; Henze et al. 2010, 2011, 2014). Most of these observation focused on the central region of M 31. A large *XMM-Newton* survey, covering the entire D₂₅ ellipse of M 31, has been presented by Stiele et al. (2011).

The X-ray source population of M 31 comprises super-soft sources (the X-ray counterparts of optical novae; e.g. Henze et al. 2014, and references therein), supernova remnants (e.g. Sasaki et al. 2012), and X-ray binaries. Regarding X-ray binaries, most sources have been classified based on correlations with lists of globular clusters, fewer through the detection of long-term variability (e.g. Williams et al. 2006; Trudolyubov et al. 2006; Stiele et al. 2008; Hofmann et al. 2013), and only a few sources through the detection of short-term variability features, characteristic for X-ray binaries (Barnard et al. 2003; Pietsch & Haberl 2005).

* E-mail: hstiele@mx.nthu.edu.tw

Table 1. Details of *NuSTAR* observations included in this study

#	Obs. id.	Date	Exp. [s]	Field
1	50026001002	2015-02-06	106386	M1
2	50026001004	2015-03-01	104295	M1
3	50111001002	2015-06-26	104123	A
4	50111001002	2015-07-25	52232	A
5	50111001004	2015-08-01	71376	A
6	50101001002	2015-09-13	98550	Bulge

In Stiele et al. (2011) 65% of the sources could have only been classified as “hard” sources, i.e. it is not possible to decide whether these sources are X-ray binaries or Crab-like supernova remnants in M 31 or AGN in the background. This confusion is partially caused by the fact that the averaged X-ray spectra of these sources at energies below 10 keV, the ones covered by the X-ray satellites mentioned above, are quite similar.

In this paper, we make use of archival *NuSTAR* data of M 31, that cover energies between 3 and 80 keV, and that allow us to study the X-ray emission of individual sources in M 31, to investigate the X-ray source population of M 31 in this energy range. Maccarone et al. (2016) investigated joint *Swift* and *NuSTAR* spectra of five globular cluster sources in M 31, and suggested that these sources are neutron star X-ray binaries. Our study, which comprises a bigger data sample, includes four of their sources.

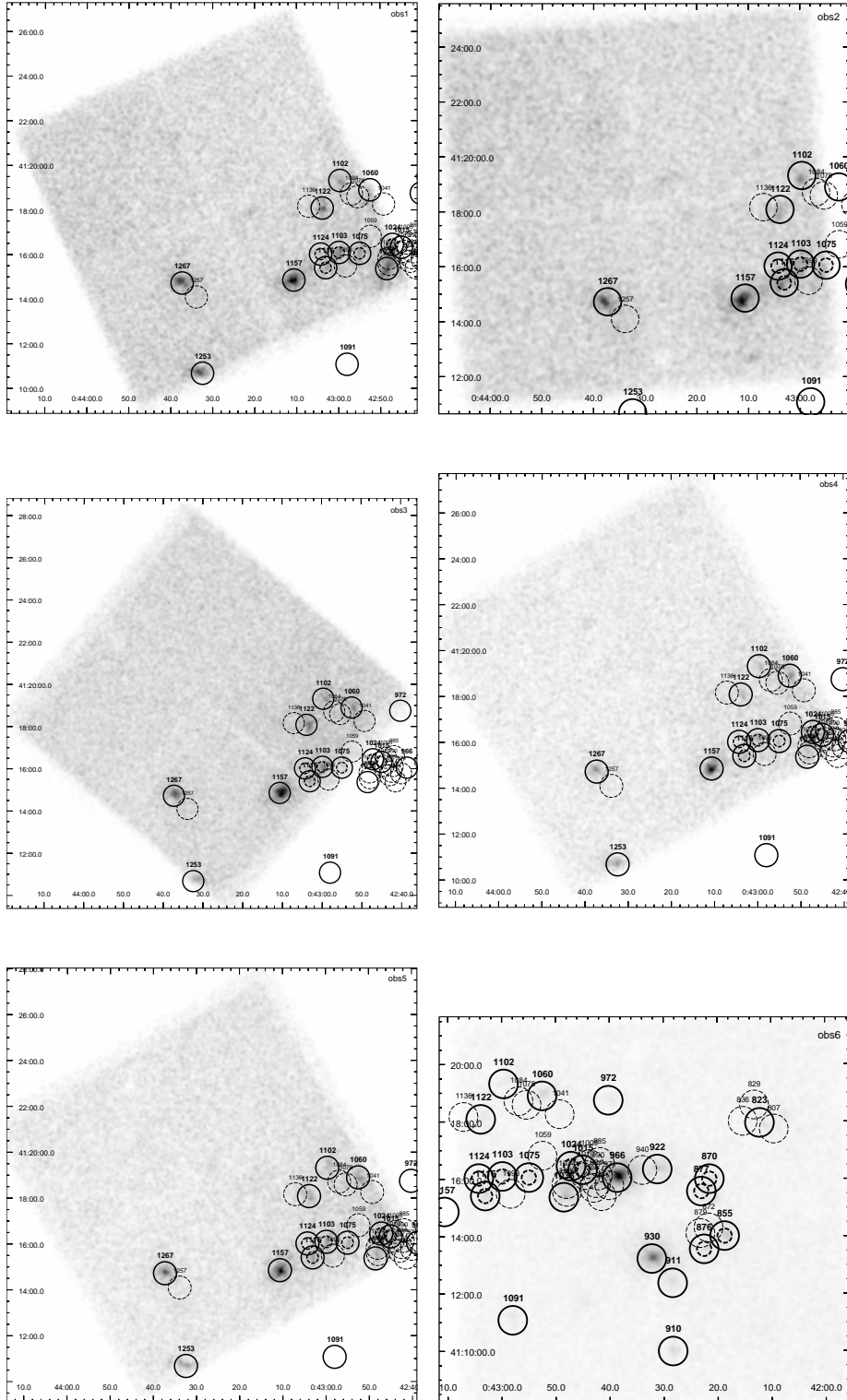


Figure 1. Images of the *NuSTAR*/FPMA data. Sources detected by *XMM-Newton* (Stiele et al. 2011) for which we found a *NuSTAR* counterpart (see Sect. 2) are indicated by black circles. Nearby *XMM-Newton* sources, which do not have a *NuSTAR* counterpart according to our selection criteria are marked as dashed circles. For sources with *NuSTAR* counterpart where source regions of 30'' overlap each other, we also indicate regions of 15'' using dashed circles.

Table 2. List of sources included in this study

Scr. ID [SPH11]	R.A.	Dec.	P _{err} arcsec	L [†] erg/s	L [†] _{err} erg/s	Class	Remark
807	00 42 9.53	+41 17 44.6	1.81	3.54E+35	1.16E+34	<GIC>	mita 140
823	00 42 12.17	+41 17 57.5	1.78	6.60E+35	1.16E+34	<GIC>	Bo 078
829	00 42 13.17	+41 18 35.1	1.73	3.60E+36	2.90E+34	<hard>	[SK98] 194
836	00 42 15.28	+41 18 0.9	2.24	5.85E+34	4.64E+33	<hard>	
855	00 42 18.71	+41 14 01.0	1.73	2.44E+36	2.32E+34	GIC	Bo 086
870	00 42 21.51	+41 16 00.3	1.74	1.33E+36	1.74E+34	<hard>	
872	00 42 21.68	+41 14 18.2	1.82	2.90E+35	5.79E+33	<GIC>	type I X-ray burst [PH2005]
876	00 42 22.51	+41 13 33.5	1.74	9.85E+35	1.16E+34	<hard>	
877	00 42 23.00	+41 15 34.3	1.72	6.20E+36	2.90E+34	<hard>	XRB in [PFH2005]
879	00 42 23.2	+41 14 6.5	1.79	2.06E+35	5.79E+33	<hard>	
910	00 42 28.31	+41 09 59.9	1.75	1.20E+36	1.74E+34	<XRB>	
911	00 42 28.37	+41 12 22.6	1.72	3.18E+36	2.32E+34	<hard>	
922	00 42 31.16	+41 16 20.7	1.73	2.90E+36	2.32E+34	<hard>	
930	00 42 32.21	+41 13 13.5	1.72	1.82E+36	1.74E+34	<hard>	
940	00 42 33.93	+41 16 18.8	1.8	3.51E+35	5.79E+33	<hard>	
966	00 42 38.61	+41 16 03.0	1.72	2.03E+37	5.21E+34	XRB	Z-source LMXRB [BKO2003]
972	00 42 40.22	+41 18 44.9	1.8	2.86E+35	5.79E+33	<hard>	
981	00 42 41.49	+41 15 24.2	1.88	2.92E+35	1.16E+34	GIC	Bo 124
985	00 42 41.85	+41 16 35.8	1.74	4.03E+36	4.06E+34	XRB	LMXRB, X-ray transient, BH candidate [WGC2006] [TPC2006]
990	00 42 42.18	+41 16 7.5	1.76	2.94E+36	5.79E+34	XRB	X-ray transient, BH candidate [OBT2001] [TBP2001]
994	00 42 42.5	+41 15 51.7	1.75	8.63E+35	2.32E+34	<hard>	
997	00 42 42.92	+41 15 41.7	1.94	2.45E+35	1.16E+34	<hard>	
1005	00 42 43.82	+41 16 31.2	1.84	5.04E+35	1.16E+34	<XRB>	recurrent X-ray transient
1010	00 42 44.48	+41 16 8.4	1.79	6.20E+35	2.32E+34	<XRB>	recurrent X-ray transient; nucleus
1015	00 42 45	+41 16 19.6	1.85	7.30E+35	1.74E+34	<hard>	WSTB 37W 135
1024	00 42 47.16	+41 16 27.2	1.72	4.83E+36	2.90E+34	<XRB>	
1036	00 42 48.50	+41 15 22.2	1.73	4.72E+36	2.90E+34	<hard>	
1041	00 42 49.24	+41 18 16	1.84	2.16E+35	5.79E+33	<hard>	
1059	00 42 52.44	+41 16 49.1	1.94	3.49E+35	1.74E+34	<XRB>	X-ray transient
1060	00 42 52.50	+41 18 54.3	1.73	3.30E+36	2.32E+34	<XRB>	superburst, NS LMXRB [K2002]
1075	00 42 54.98	+41 16 03.5	1.73	3.48E+36	2.32E+34	<hard>	
1078	00 42 55.39	+41 18 35.7	1.79	3.34E+35	5.79E+33	<hard>	
1084	00 42 56.89	+41 18 43.2	2.97	4.62E+35	4.64E+34	<XRB>	X-ray transient
1091	00 42 58.01	+41 11 5.0	1.74	1.66E+36	1.74E+34	<hard>	
1093	00 42 58.36	+41 15 29.6	1.83	2.57E+35	5.79E+33	<hard>	
1102	00 42 59.65	+41 19 19.4	1.73	1.87E+36	1.74E+34	GIC	Bo 143
1103	00 42 59.90	+41 16 05.9	1.73	1.92E+36	1.74E+34	GIC	Bo 144
1116	00 43 03.08	+41 15 25.0	1.73	2.85E+36	2.32E+34	GIC	Bo 146
1122	00 43 03.89	+41 18 05.4	1.73	1.44E+36	1.74E+34	GIC	Bo 148
1124	00 43 4.27	+41 16 1.6	1.86	2.13E+35	5.79E+33	<GIC>	
1136	00 43 7.1	+41 18 10.4	1.81	4.87E+35	1.74E+34	<XRB>	
1157	00 43 10.66	+41 14 51.8	1.72	4.40E+36	2.90E+34	GIC	Bo 153
1253	00 43 32.44	+41 10 41.3	1.75	1.45E+36	2.32E+34	<hard>	
1257	00 43 33.9	+41 14 6.5	4.51	3.70E+34	5.79E+33	<hard>	
1267	00 43 37.30	+41 14 43.9	1.74	2.78E+36	2.90E+34	GIC	Bo 185

Notes:

values and classification taken from Stiele et al. (2011)

WGC2006: Williams et al. (2006), TPC2006: Trudolyubov et al. (2006), PFH2005: Pietsch et al. (2005), PH2005: Pietsch & Haberl (2005), BKO2003: Barnard et al. (2003), K2002: Kaaret (2002), OBT2001: Osborne et al. (2001), TBP2001: Trudolyubov et al. (2001), SK98: Shokin & Kulagina (1998), mita: Magnier (1993), WSTB 37W: Walterbos et al. (1985)

†: luminosity in the 0.2 – 4.5 keV band, assuming a distance to M 31 of 780 kpc
italic source IDs indicate sources for which we found *NuSTAR* counterparts

2 OBSERVATION AND DATA ANALYSIS

Details on the observations used in this study are given in table 1. We analysed the *NuSTAR* data using the NuSTARDAS tools nupipeline and nuproducts. We loaded the cleaned images produced by nupipeline into ds9 and used the source catalogue of

the deep *XMM-Newton* survey of M 31 (Stiele et al. 2011) as a reference source list to select by eye possible *NuSTAR* candidates of the *XMM-Newton* sources. We also selected all sources from the *XMM-Newton* source catalogue identified or classified as X-ray binary, globular cluster or “hard” that are located so close to our selected *NuSTAR* candidates that extraction regions with a radius

Table 3. Count rate ratios and significance of sources included in this study

Scr. ID [SPH11]	region 15''		region 30''	
	R	Sig	R	Sig
807	1.195 ± 0.001	1.824 ± 0.089	1.255 ± 0.043	4.277 ± 0.806
823	1.313 ± 0.006	2.942 ± 0.094	1.326 ± 0.018	5.440 ± 0.164
829	1.152 ± 0.018	1.418 ± 0.166	1.186 ± 0.067	3.144 ± 0.984
836	0.984 ± 0.103	-0.209 ± 0.916	0.986 ± 0.024	-0.271 ± 0.446
855	1.864 ± 0.025	8.034 ± 0.268	1.620 ± 0.039	10.637 ± 0.516
870	1.313 ± 0.102	3.371 ± 1.015	1.676 ± 0.213	10.643 ± 2.415
872	1.040 ± 0.086	0.400 ± 0.909	1.054 ± 0.074	1.066 ± 1.494
876	1.639 ± 0.112	5.837 ± 0.710	1.223 ± 0.001	4.480 ± 0.103
877	1.247 ± 0.080	2.586 ± 0.807	1.532 ± 0.128	8.810 ± 1.864
879	0.895 ± 0.084	-1.281 ± 1.049	1.042 ± 0.009	0.910 ± 0.200
910	1.836 ± 0.401	6.196 ± 2.279	1.562 ± 0.077	8.134 ± 0.835
911	1.418 ± 0.115	4.042 ± 0.984	1.132 ± 0.020	2.711 ± 0.320
922	1.444 ± 0.151	5.477 ± 1.693	1.669 ± 0.237	12.429 ± 3.343
930	2.112 ± 0.023	15.820 ± 0.387	3.211 ± 0.319	33.918 ± 3.003
940	1.025 ± 0.010	0.358 ± 0.128	0.791 ± 0.049	-7.417 ± 1.895
966	2.347 ± 0.101	22.321 ± 1.152	3.116 ± 0.252	41.902 ± 2.000
971	0.826 ± 0.026	-3.955 ± 0.467	1.748 ± 0.054	20.122 ± 1.663
972	1.341 ± 0.203	2.677 ± 1.484	1.215 ± 0.016	3.385 ± 0.213
981	0.856 ± 0.042	-2.025 ± 0.454	0.686 ± 0.077	-11.287 ± 2.774
985	0.848 ± 0.053	-2.852 ± 1.126	0.841 ± 0.053	-6.326 ± 2.197
990	1.057 ± 0.021	1.063 ± 0.356	1.073 ± 0.002	2.664 ± 0.101
994	1.015 ± 0.032	0.276 ± 0.568	0.907 ± 0.057	-3.593 ± 2.226
997	0.997 ± 0.017	-0.029 ± 0.267	0.858 ± 0.055	-5.136 ± 1.961
1005	1.085 ± 0.039	1.465 ± 0.669	1.184 ± 0.022	5.810 ± 0.704
1010	1.029 ± 0.050	0.527 ± 0.910	1.264 ± 0.053	8.029 ± 1.468
1015	1.178 ± 0.002	3.071 ± 0.020	1.427 ± 0.020	12.089 ± 0.474
1024	1.418 ± 0.059	6.279 ± 0.905	1.526 ± 0.111	13.179 ± 2.331
1036	1.533 ± 0.182	4.390 ± 1.602	1.398 ± 0.328	6.568 ± 4.882
1041	1.007 ± 0.215	0.136 ± 1.337	0.948 ± 0.162	-0.755 ± 2.408
1059	1.062 ± 0.124	0.373 ± 0.981	0.908 ± 0.064	-1.833 ± 1.407
1060	1.529 ± 0.175	4.387 ± 1.445	1.613 ± 0.154	8.385 ± 2.127
1075	1.404 ± 0.124	3.443 ± 1.044	1.201 ± 0.054	3.455 ± 1.121
1078	1.047 ± 0.101	0.407 ± 0.874	1.061 ± 0.152	0.720 ± 2.606
1084	0.991 ± 0.130	-0.171 ± 1.103	0.937 ± 0.150	-1.433 ± 2.594
1091	1.251 ± 0.183	2.016 ± 1.387	1.342 ± 0.031	5.118 ± 0.404
1093	0.998 ± 0.115	-0.077 ± 1.088	0.936 ± 0.131	-1.432 ± 2.935
1102	1.439 ± 0.174	3.586 ± 1.274	1.391 ± 0.202	5.719 ± 2.399
1103	1.500 ± 0.200	4.246 ± 1.329	1.309 ± 0.065	5.242 ± 1.016
1116	1.405 ± 0.128	3.557 ± 1.116	1.323 ± 0.222	5.315 ± 3.527
1122	1.468 ± 0.167	3.943 ± 1.408	1.476 ± 0.121	7.069 ± 2.107
1124	1.529 ± 0.175	4.387 ± 1.445	1.613 ± 0.154	8.385 ± 2.127
1136	1.016 ± 0.123	0.011 ± 1.017	1.021 ± 0.084	0.207 ± 1.453
1157	2.216 ± 0.246	11.073 ± 1.440	2.402 ± 0.213	18.653 ± 1.955
1253	1.878 ± 0.233	6.005 ± 1.675	2.127 ± 0.327	11.336 ± 3.689
1257	0.971 ± 0.086	-0.320 ± 0.741	0.891 ± 0.067	-1.885 ± 1.163
1267	1.848 ± 0.197	7.256 ± 1.293	2.017 ± 0.224	13.014 ± 1.751

of 30'' overlap each other. For all these sources (listed in Table 2) we extracted source counts from regions of 15'' and 30'' radius located at the known position of each source, and corresponding “background” counts from annulus regions with $20'' < r < 25''$ and $45'' < r < 54''$, respectively. We then derived the ratio of the source to the background counts $R = C_{\text{src}}/C_{\text{bkg}}$, and the significance of the count rate difference:

$$\text{Sig} = \frac{C_{\text{src}} - C_{\text{bkg}}}{\sqrt{\sigma_{\text{src}}^2 + \sigma_{\text{bkg}}^2}} \quad (1)$$

where σ_{src} and σ_{bkg} are the errors of the source and background count rates, respectively. We derived these values for individual

FPMs, as well as averages for all FPMs that cover a source position (Table 3), where we excluded FPMs where the source is located so close to the edge of the field of view that any of the extraction regions is only partially covered.

Images of the *NuSTAR*/FPMA and B data, overlaid with source regions are shown in Figs. 1, 2. Sources [SPH11] 910, 911, 930, 972, 1091, 1157, and 1253 do not overlap with any other *XMM-Newton* source. Ignoring all “sources” where $R < 1$, sources [SPH11] 922, 1036, 1102, and 1267 do also not overlap with an other source. Regarding the remaining sources we included those sources in our study which have averaged significances bigger than three (including errors) for the small and big extraction regions.

Table 4. List of background subtracted NuSTAR FPMA/B source counts (in units of $\times 10^{-3}$ cts/s) from a source extraction region of $30''$.

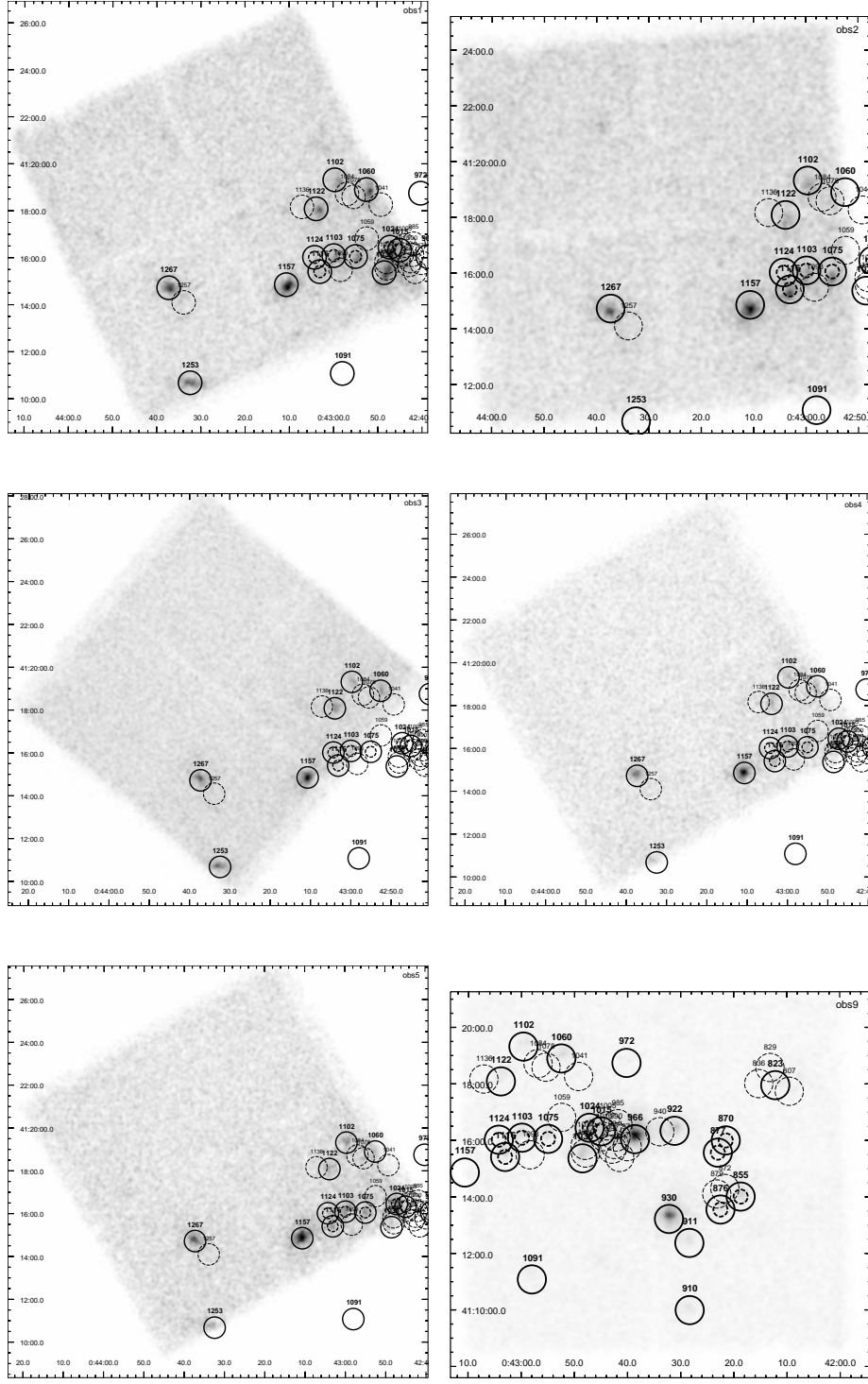
[SPH11]	FPM	obs. 1	obs. 2	obs. 3	obs. 4	obs. 5	obs. 6
823	A	—	—	—	—	—	3.28 ± 0.32
	B	—	—	—	—	—	3.01 ± 0.31
855	A	—	—	—	—	—	5.83 ± 0.39
	B	—	—	—	—	—	5.44 ± 0.39
870	A	—	—	—	—	—	5.44 ± 0.36
	B	—	—	—	—	—	5.93 ± 0.35
876	A	—	—	—	—	—	4.49 ± 0.37
	B	—	—	—	—	—	4.03 ± 0.36
877	A	—	—	—	—	—	4.43 ± 0.39
	B	—	—	—	—	—	3.66 ± 0.35
910	A	—	—	—	—	—	2.55 ± 0.33
	B	—	—	—	—	—	2.75 ± 0.32
911	A	—	—	—	—	—	4.10 ± 0.37
	B	—	—	—	—	—	3.12 ± 0.36
922	A	—	—	—	—	—	8.49 ± 0.42
	B	—	—	—	—	—	9.44 ± 0.45
930	A	—	—	—	—	—	23.52 ± 0.57
	B	—	—	—	—	—	27.23 ± 0.61
966	A	—	—	—	—	—	40.03 ± 0.71
	B	—	—	—	—	—	39.24 ± 0.71
972	A	—	—	—	—	—	1.08 ± 0.29
	B	—	—	—	—	—	1.20 ± 0.29
1015	A	—	—	—	5.73 ± 0.54	5.30 ± 0.45	19.82 ± 0.53
	B	—	—	—	2.83 ± 0.37	2.74 ± 0.31	19.83 ± 0.53
1024	A	—	—	—	6.32 ± 0.55	5.40 ± 0.47	15.92 ± 0.49
	B	—	—	—	4.62 ± 0.49	4.29 ± 0.42	17.71 ± 0.51
1036	A	5.14 ± 0.34	—	—	3.90 ± 0.45	3.88 ± 0.38	10.99 ± 0.44
	B	7.31 ± 0.37	—	—	1.09 ± 0.24	1.14 ± 0.25	9.12 ± 0.40
1060	A	—	—	2.72 ± 0.38	4.03 ± 0.52	3.60 ± 0.43	4.91 ± 0.35
	B	—	—	3.32 ± 0.37	2.89 ± 0.41	2.30 ± 0.30	4.48 ± 0.36
1075	A	2.01 ± 0.30	—	—	2.65 ± 0.50	1.45 ± 0.41	4.36 ± 0.36
	B	3.08 ± 0.31	—	—	3.38 ± 0.48	2.40 ± 0.42	4.47 ± 0.36
1091	A	—	—	—	—	—	1.69 ± 0.29
	B	—	—	—	—	—	1.86 ± 0.30
1102	A	1.45 ± 0.28	1.45 ± 0.31	2.51 ± 0.38	1.57 ± 0.47	1.41 ± 0.41	1.65 ± 0.30
	B	2.21 ± 0.31	2.10 ± 0.34	2.13 ± 0.36	1.45 ± 0.46	3.00 ± 0.40	2.40 ± 0.32
1103	A	3.20 ± 0.29	3.38 ± 0.32	4.07 ± 0.36	5.09 ± 0.52	5.11 ± 0.44	4.77 ± 0.36
	B	3.83 ± 0.31	3.91 ± 0.34	2.29 ± 0.27	5.00 ± 0.49	4.75 ± 0.41	6.01 ± 0.38
1116	A	2.25 ± 0.28	4.09 ± 0.33	3.05 ± 0.34	3.67 ± 0.49	4.63 ± 0.43	4.90 ± 0.36
	B	2.19 ± 0.28	6.02 ± 0.36	1.53 ± 0.26	3.21 ± 0.45	3.59 ± 0.39	5.63 ± 0.36
1122	A	2.17 ± 0.30	1.53 ± 0.31	4.29 ± 0.40	1.90 ± 0.48	2.10 ± 0.42	2.31 ± 0.31
	B	3.27 ± 0.33	1.82 ± 0.32	4.01 ± 0.38	2.18 ± 0.48	2.31 ± 0.39	2.32 ± 0.32
1124	A	1.24 ± 0.26	1.96 ± 0.30	1.72 ± 0.34	1.93 ± 0.45	3.64 ± 0.37	2.19 ± 0.32
	B	1.30 ± 0.26	1.72 ± 0.30	1.54 ± 0.33	2.13 ± 0.43	3.28 ± 0.38	4.62 ± 0.36
1157	A	7.82 ± 0.36	8.26 ± 0.39	13.63 ± 0.47	13.98 ± 0.65	12.74 ± 0.54	—
	B	8.46 ± 0.36	9.18 ± 0.39	11.64 ± 0.44	12.70 ± 0.63	12.78 ± 0.54	—
1253	A	4.63 ± 0.28	—	2.26 ± 0.23	5.10 ± 0.40	4.46 ± 0.33	—
	B	5.25 ± 0.31	—	6.09 ± 0.37	2.52 ± 0.26	2.73 ± 0.25	—
1267	A	5.38 ± 0.34	5.56 ± 0.35	6.85 ± 0.37	5.96 ± 0.47	7.04 ± 0.44	—
	B	6.29 ± 0.32	5.51 ± 0.34	7.25 ± 0.39	6.96 ± 0.52	6.58 ± 0.45	—

For all selected sources (indicated by an *italic* source ID in the first column of Table 2) we extracted source photons from a circular region with a radius of $30''$ located at the known position of each source to derive X-ray spectra. For sources [SPH11] 855, 870, 876, 877, 1015, 1024, 1075, 1103, 1116, 1124 which overlap with at least one other source we also used the smaller radius of $15''$. A circular background region with a radius of $30''$ located close to the source on the same detector and free of source photons was also

extracted. Background subtracted source counts in the $3 - 78$ keV band obtained with nuproducts are given in Table 4.

3 RESULTS

Selecting the sources, we noticed that there are only previously known sources, with a brightness comparable (or even brighter) than the selected sources, in the NuSTAR data. The source IDs used

**Figure 2.** Images of the *NuSTAR*/FPMB data. See Fig. 1.

in this paper are from the *XMM-Newton* catalogue of [Stiele et al. \(2011\)](#).

3.1 Hardness ratio diagram

We used isis (V. 1.6.2; [Houck & Denicola 2000](#)) to obtain estimates of the background subtracted source count rates from the *NuSTAR* energy spectra in band 1 (3 – 10 keV), band 2 (10 – 20 keV), and band 3 (20 – 78 keV) combining data of both focal plane instruments. We derived two hardness ratios (HR) and errors for each

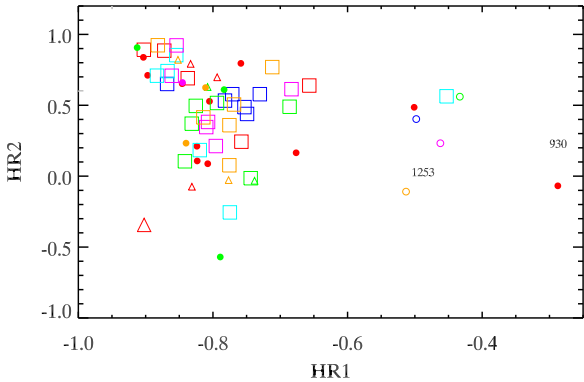


Figure 3. Hardness ratio diagram for all sources. To keep the plot less busy no error bars are shown. Error bars are given in the HR diagrams of individual sources (Fig. 4). Counterparts of globular clusters are marked with squares, those of X-ray binaries with triangles. Big symbols indicate identified sources, while small symbols indicate candidates (as given in Table 2). Hardness ratios of [SPH11] 1253 are marked with open circles. Different colours indicate different observations: obs. 1: magenta; obs. 2: cyan; obs. 3: blue; obs. 4: green; obs. 5: orange; obs. 6: red.

source in each observation using the following equations:

$$\text{HR}i = \frac{B_{i+1} - B_i}{B_{i+1} + B_i} \quad \text{and} \quad \text{EHR}i = 2 \frac{\sqrt{(B_{i+1}EB_i)^2 + (B_iEB_{i+1})^2}}{(B_{i+1} + B_i)^2} \quad (2)$$

for $i = 1, 2$, where B_i and EB_i denote count rates and corresponding errors in the energy band i .

In the HR diagram (Fig. 3), sources that are already classified as X-ray binaries or globular cluster sources are located at $\text{HR}1 \leq -0.6$. For the 13 sources that were in the field of view of more than one observation, we show HR diagrams of each source in Fig. 4. From these diagrams we see that for all sources the hardness ratios obtained from different observations do agree within error bars. The four observations of [SPH11] 1253 give slightly higher $\text{HR}1$ values and the $\text{HR}1$ value of [SPH11] 930 is even higher. The location of [SPH11] 930 in the HR diagram in comparison with the location of sources classified as X-ray binaries suggests that the X-ray spectral properties of [SPH11] 930 differ from those classified as X-ray binary. Source [SPH11] 1122 shows the strongest evolution in $\text{HR}1$. In obs. 2, it shows the highest $\text{HR}1$ value, which is comparable to those of [SPH11] 1253. The results of a more detailed spectral study (see Sect. 3.2) confirm that [SPH11] 1122 is harder in obs. 2 than in any other observation. Another source with $\text{HR}1$ values close to those of [SPH11] 1253 is [SPH11] 972, which is also fainter than [SPH11] 1253. In the region where the classified X-ray binaries are located there are nine sources ([SPH11] 870, 876, 877, 911, 922, 1015, 1036, 1075, 1091) that have only been classified as “hard” in Stiele et al. (2011). Source [SPH11] 876 has the highest and [SPH11] 1075 the lowest $\text{HR}1$ value of these nine sources. Source [SPH11] 1015 has been covered by three observations, and sources [SPH11] 1036 and 1075 have been covered by four observations. The nine “hard” sources located at $\text{HR}1 \leq -0.6$ are possible X-ray binary candidates.

3.2 Spectral properties

To investigate this possibility further, we fitted simultaneously the FPMA and FPMB energy spectra of each source within XSPEC

(V. 12.8.2; Arnaud 1996) in the 3 – 78 keV range, grouping the data to a minimum of 20 counts in each bin. We use the following three simple models, which have also been used in Maccarone et al. (2016), to fit the data: powerlaw, diskbb (Mitsuda et al. 1984), and comptt (Titarchuk 1994), including Galactic foreground absorption using TBabs (Wilms et al. 2000). The obtained best fit parameters are given in Table 5, together with luminosities and errors, derived using the cflux model. Four spectra with the best fit models and residuals are shown in Fig. 5. We selected the brightest observations of [SPH11] 1075, 1157 (the brightest globular cluster source in our sample) and 1253, and the faintest observation of 1102 (the faintest globular cluster source in our sample). We find that most sources have a photon index above or close to two, similar to what has been found in Maccarone et al. (2016). Exceptions are [SPH11] 930 with $\Gamma = 1.22 \pm 0.04$ and [SPH11] 1253 with a photon index around 1.5. We can also confirm another result of Maccarone et al. (2016), that for most observations the comptt model provides a statistically better fit than a power law.

For sources observed more than once we can investigate the evolution of the spectral parameters. For almost all observations the value of the cross-calibration constant is independent of the spectral model used. For most sources the normalisations of the power law and of the disk blackbody show a similar evolution, and the evolution of the photon index and inner disc temperature is anti-correlated. The photon index and inner disc temperature and radius are constant within errors. Exceptions are [SPH11] 1122 (obs 2/3) and [SPH11] 1267 (obs 4). In general, the seed temperature in the comptt model is lower than the disc temperature in the diskbb model and it shows a different evolution. While a disc temperature of ~ 2 keV is quite high compared to values obtained from Galactic X-ray binaries using multi-component spectral models, it is in agreement with the values reported in Maccarone et al. (2016). Regarding correlations between spectral parameters and source flux, we do not find any overall correlation of any specific spectral parameter with flux. The evolution of the photon index with luminosity is shown in Fig. 6. Only [SPH11] 1157 and 1267 are getting harder when they get brighter. For these two sources we also find that the disc temperature increases when they get brighter. [SPH11] 1267 shows a decreasing radius with increasing flux, while the radius of [SPH11] 1157 is constant.

3.3 Long term light curves

For the 13 sources that were in the field of view of more than one observation, we prepared long term light curves. We derived the fluxes from the spectral fits adding the cflux component to each spectral model with all parameters fixed to their best fit value. Fluxes are derived in the 3 – 78 keV band and converted to luminosities assuming a distance of 780 kpc. The obtained light curves are shown in Fig. 7. Following Stiele et al. (2011) we determine the variability factor, the ratio of the maximum and minimum luminosity, $Var = L_{\max}/L_{\min}$, and the significance of the luminosity difference:

$$Sig = \frac{L_{\max} - L_{\min}}{\sqrt{\sigma_{\max}^2 + \sigma_{\min}^2}} \quad (3)$$

where σ_{\max} and σ_{\min} are the errors of the maximum and minimum luminosity (ignoring uncertainties on the distance), respectively. Apart from the brightest source ([SPH11] 1253) the overall evolution of the luminosity with time is consistent between the different models. For [SPH11] 1015, 1024, 1060, 1102, 1103, 1122, 1124,

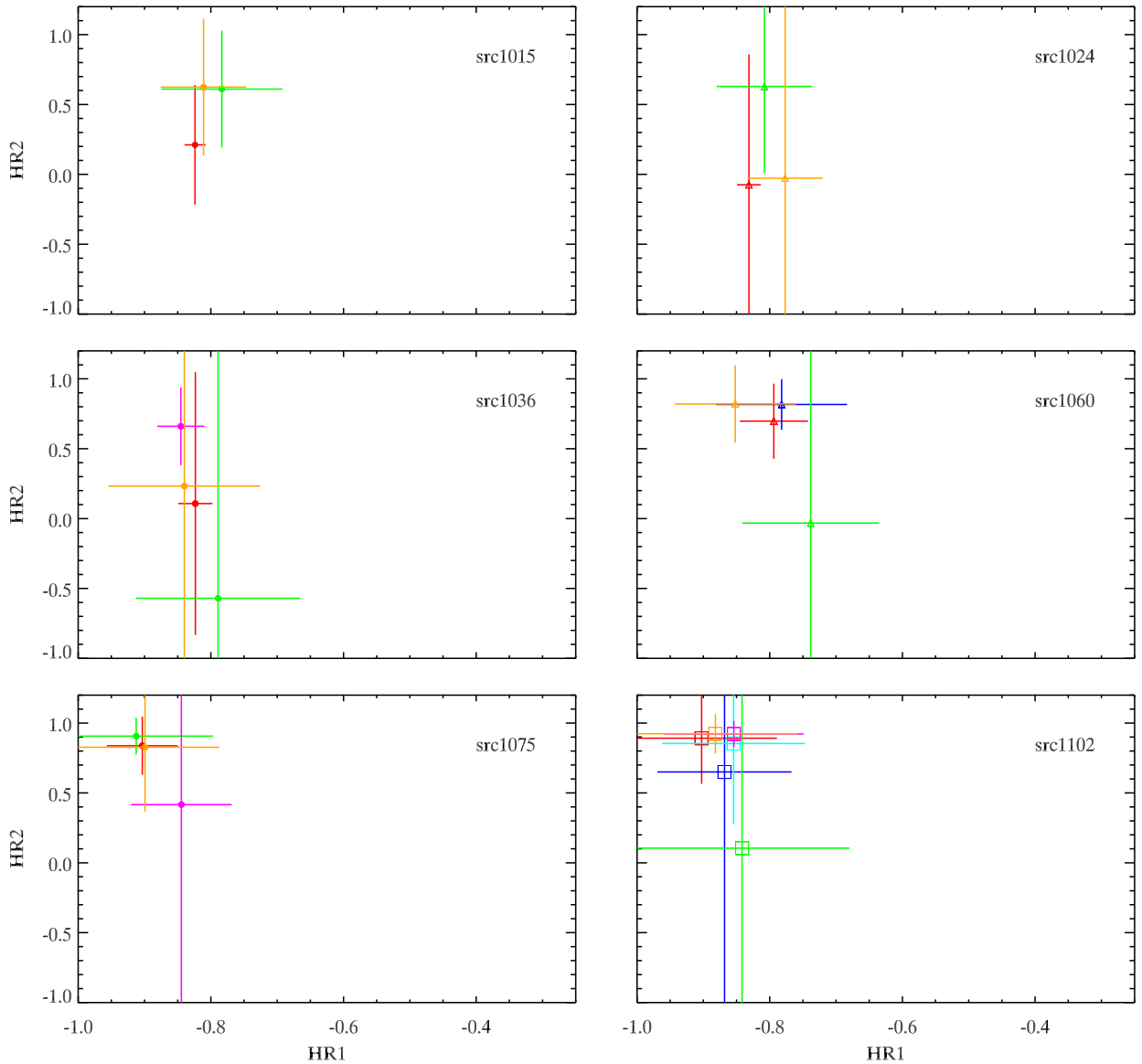


Figure 4. Hardness ratio diagrams of the 13 sources that were observed more than once. Different colours indicate different observations; different symbols indicate different source types (see Fig. 3).

1157 and 1267 we observe an overall flux increase, while [SPH11] 1036 and 1253 show an overall decreasing flux. For [SPH11] 1102 and 1122 there are two observations (obs. 4, 5) where the flux deviates from the overall increase, as it is lower in these two observations. For [SPH11] 1103 and 1157 the flux in the first two observations is lower than in the remaining observations. However, the variability factor is rather low. For most sources the variability factor is about 1 – 2, and it is below 5 for all sources. For most sources the significance of variability is $\lesssim 3$, only [SPH11] 1157 has $Sig > 5$. For [SPH11] 1015, 1024, 1075, 1103, 1116, and 1124 we also show luminosities derived from source extraction regions of $15''$. For most observations the overall evolution of the luminosity does not depend on the size of the extraction region. An excep-

tion is [SPH11] 1124 where the evolution of the luminosity in the last four observations does not agree with each other. For most observations the luminosities derived from the $15''$ regions are lower than those derived from the $30''$ regions. In case the evolution of the luminosities does not depend on the size of the extraction region, the lower luminosities from the $15''$ regions imply that we miss source flux using these extraction regions, while the bigger extraction regions are still dominated by the source flux and contribution from nearby sources does not seem to affect the fluxes obtained.

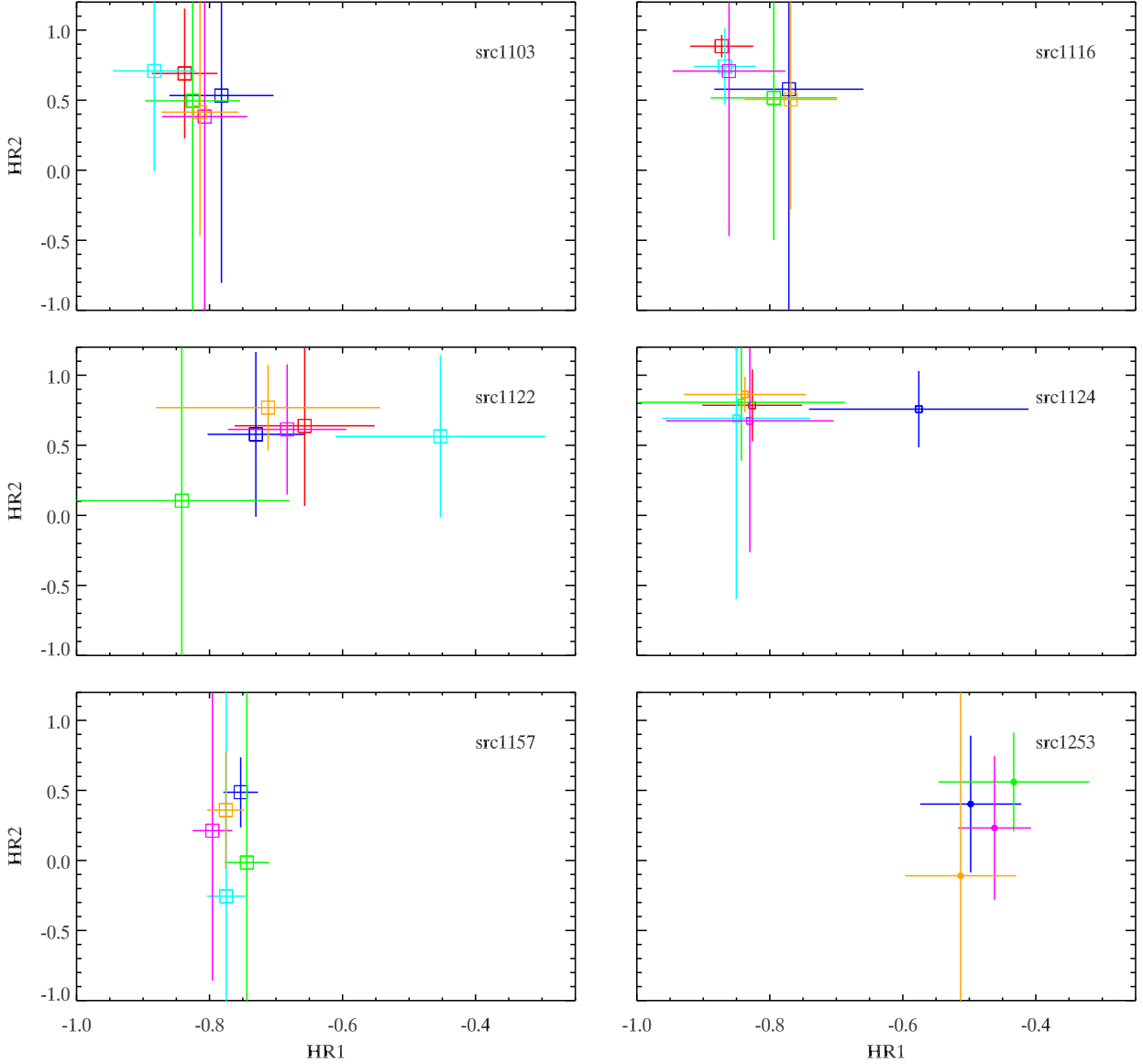


Figure 4. continued

4 DISCUSSION

We analysed *NuSTAR* data of M 31 taken between February and September 2015. Comparing with the *XMM-Newton* source list presented in Stiele et al. (2011) we find that all sources visible in the *NuSTAR* data have already been seen with *XMM-Newton*, i.e. the *NuSTAR* data do not contain any transient source that was not active at the time of the *XMM-Newton* data analysed by Stiele et al. (2011). Investigating hardness ratios we find that most sources are located in a certain region of the hardness ratio diagram. More detailed spectral fitting confirms that most sources have similar spectral properties. This suggests that [SPH11] 922, 1015, 1036, 1075, which have only been classified as “hard” in Stiele et al. (2011) are good candidates for being X-ray binaries, as their spectral proper-

ties are quite similar to the ones of the identified X-ray binaries included in our source sample.

Sources [SPH11] 930 and [SPH11] 1253 are located at higher HR1 values than the identified X-ray binaries, and our more detailed spectral investigation confirms that these two sources have harder spectra than the identified X-ray binaries. There are several possibilities why the spectra of sources [SPH11] 930 and [SPH11] 1253 differ from those of the identified X-ray binaries. One possibility is that these two sources are background AGN, not belonging to the X-ray binary population of M 31. Another possibility is that these two sources are X-ray binaries observed in a (much) harder state than the identified X-ray binaries. Hofmann et al. (2013) suggest [SPH11] 930 to be an X-ray binary candidate based on the long-term variability observed in *Chandra* HRC-I observations.

Table 5. Spectral parameters obtained by fitting the *NuSTAR* spectra. Luminosities in units of 10^{36} erg/s. This is a sample of the full table, which is available with the electronic version of the article.

src.	obs.	Γ $C_{\text{FPMB};\text{ctt}}$	N_{pl} $\chi^2_{\text{pl}}/\text{dof}$	$C_{\text{FPMB};\text{pl}}$ $\chi^2_{\text{dbb}}/\text{dof}$	T_{in} [keV] $\chi^2_{\text{ctt}}/\text{dof}$	N_{dbb} L_{pl}	$C_{\text{FPMB};\text{dbb}}$ L_{dbb}	T_0 [keV] L_{ctt}	T_{e} [keV]	τ	N_{ctt}
823	6	$2.40^{+0.25}_{-0.24}$ $0.86^{+0.19}_{-0.18}$	$3.51^{+2.00}_{-1.25} E - 04$ 60.15/58	$0.86^{+0.19}_{-0.15}$ 61.02/58	$2.40^{+0.41}_{-0.33}$ 58.24/56	$8.70^{+7.95}_{-4.24} E - 04$ 3.78/ $^{+0.37}_{-0.31}$	$0.87^{+0.19}_{-0.16}$ 2.37/ $^{+0.23}_{-0.17}$	$4.76^{+4.53}_{-4.76} E - 01$ 2.61/ $^{+0.26}_{-0.29}$	$2.89^{+84.01}_{-0.97}$	$5.52^{+4.48}_{-5.52}$	$6.12^{+329.60}_{-6.12} E - 05$
855	6	$2.39^{+0.18}_{-0.18}$ $0.99^{+0.17}_{-0.17}$	$3.86^{+1.64}_{-1.14} E - 04$ 31.79/33	$0.94^{+0.18}_{-0.15}$ 28.27/33	$2.80^{+0.40}_{-0.34}$ 24.73/31	$5.42^{+0.51}_{-2.39} E - 04$ 4.33/ $^{+0.37}_{-0.37}$	$0.91^{+0.17}_{-0.15}$ 2.02/ $^{+0.16}_{-0.20}$	$2.02^{+0.49}_{-0.49} E - 03$ 3.22/ $^{+0.28}_{-0.28}$	$3.31^{+0.39}_{-0.35}$	$5.30^{+0.66}_{-0.56}$	$8.00^{+538020.00}_{-0.71} E - 03$
870	6	$2.45^{+0.15}_{-0.15}$ $1.03^{+0.15}_{-0.15}$	$4.27^{+1.29}_{-1.00} E - 04$ 105.80/79	$1.10^{+0.15}_{-0.13}$ 87.77/79	$2.40^{+0.22}_{-0.20}$ 4.16/ $^{+0.27}_{-0.27}$	$1.06^{+0.34}_{-0.34} E - 03$ 2.89/ $^{+0.18}_{-0.19}$	$1.02^{+0.14}_{-0.12}$ 1.43/ $^{+0.04}_{-0.43}$	$1.43^{+0.04}_{-0.13} E - 01$ 2.91/ $^{+0.19}_{-0.19}$	$2.14^{+0.67}_{-0.38}$	$8.12^{+4.43}_{-2.44}$	$2.00^{+1668.80}_{-0.19} E - 03$
876	6	$2.06^{+0.26}_{-0.26}$ $0.95^{+0.26}_{-0.26}$	$1.28^{+0.99}_{-0.52} E - 04$ 21.81/24	$0.95^{+0.26}_{-0.20}$ 26.74/24	$3.79^{+1.02}_{-0.76}$ 3.26/ $^{+0.37}_{-0.37}$	$9.33^{+0.90}_{-5.68} E - 05$ 1.93/ $^{+0.25}_{-0.27}$	$0.98^{+0.21}_{-0.21}$ 2.42/ $^{+0.28}_{-0.28}$	$4.64^{+3.19}_{-3.64} E - 01$ 2.95/ $^{+0.59}_{-0.95}$	$5.99^{+160.50}_{-2.75}$	$3.86^{+3.00}_{-3.80}$	$1.71^{+59.76}_{-1.71} E - 05$
877	6	$2.35^{+0.23}_{-0.21}$ $1.02^{+0.21}_{-0.18}$	$2.80^{+1.39}_{-0.94} E - 04$ 82.51/74	$1.03^{+0.22}_{-0.18}$ 81.92/74	$2.69^{+0.44}_{-0.36}$ 3.40/ $^{+0.32}_{-0.32}$	$4.83^{+0.88}_{-0.77} E - 04$ 2.23/ $^{+0.21}_{-0.21}$	$1.01^{+0.37}_{-0.18}$ 2.43/ $^{+0.23}_{-0.23}$	$9.95^{+165.89}_{-0.95} E - 03$ 3.26/ $^{+7.42}_{-1.03}$		$5.26^{+3.27}_{-3.09}$	$1.66^{+0.30}_{-1.66} E - 03$

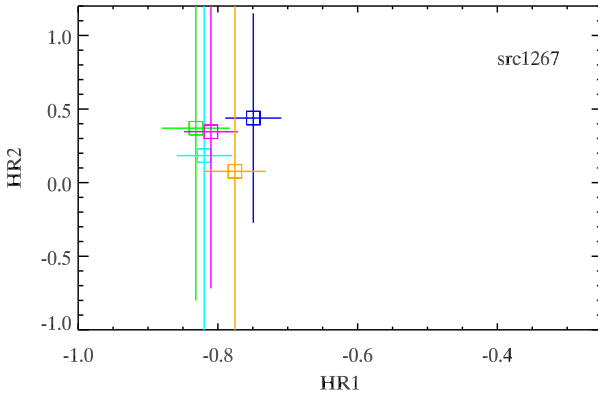


Figure 4. continued

[Yukita et al. \(2017\)](#) reported the identification of a bright hard X-ray source dominating the M 31 bulge above 25 keV (the *NuSTAR* counterpart of [SPH11] 930), which is the counterpart to Swift J0042.6+4112, a possible X-ray pulsar with an intermediate-mass companion or a symbiotic X-ray binary. [Marelli et al. \(2017\)](#) re-analysed archival *XMM-Newton* observation of this source and discovered periodic dips. They suggest [SPH11] 930 to be a dipping low-mass X-ray binary seen at high inclination. [Maccarone et al. \(2016\)](#) argue that X-ray binaries associated with globular clusters in M 31 are most likely containing a neutron star primary. So the harder spectra of [SPH11] 1253 can indicate that this source is a black hole X-ray binary. A photon index of ~ 1.5 , as seen in [SPH11] 1253, can be observed in the low-hard state of a black hole X-ray binary (e.g. [Stiele et al. 2013; Stiele & Kong 2016](#)). As [SPH11] 1253 is a field source the harder spectra of this source may indicate that it is a (neutron star) high-mass X-ray binary. However, it is not among the list of candidate high-mass X-ray binaries of [Shaw Greening et al. \(2009, Table 5\)](#). The long-term *XMM-Newton* light curve of [SPH11] 1253 obtained from the 0.2 – 12 keV band flux given in the 3XMM-DR6 catalogue ([Rosen et al. 2016](#)) is shown in Fig. 8. The light curve shows low (var = 1.79), but significant (sig: 8.62) variability. An interpretation as a supernova remnant is unlikely as the source shows significant variability and it is not included in the list of supernova remnants and candidates presented in [Sasaki et al. \(2012\)](#).

ACKNOWLEDGMENTS

This project is supported by the Ministry of Science and Technology of the Republic of China (Taiwan) through grants 103-2628-M-007-003-MY3, 104-281-M-007-060, 105-2112-M-007-033-MY2 and 105-2811-M-007-065. This research has made use of data obtained through the High Energy Astrophysics Science Archive Research Center Online Service, provided by the NASA/Goddard Space Flight Center. This research has made use of data obtained from the 3XMM XMM-Newton serendipitous source catalogue compiled by the 10 institutes of the XMM-Newton Survey Science Centre selected by ESA.

References

- Arnaud K. A., 1996, in G. H. Jacoby & J. Barnes ed., Astronomical Data Analysis Software and Systems V Vol. 101 of Astronomical Society of the Pacific Conference Series, XSPEC: The First Ten Years. p. 17
- Barnard R., Kolb U., Osborne J. P., 2003, A&A, 411, 553
- Collura A., Reale F., Peres G., 1990, ApJ, 356, 119
- Di Stefano R., Kong A. K. H., Garcia M. R., Barnaby P., Greiner J., Murray S. S., Primini F. A., 2002, ApJ, 570, 618
- Di Stefano R., Kong A. K. H., Greiner J., Primini F. A., Garcia M. R., Barnaby P., Massey P., Hodge P. W., Williams B. F., Murray S. S., Curry S., Russo T. A., 2004, ApJ, 610, 247
- Garcia M. R., Murray S. S., Primini F. A., Forman W. R., McClintock J. E., Jones C., 2000, ApJ, 537, L23
- Henze M., Pietsch W., Haberl F., Della Valle M., Sala G., Hatzidimitriou D., Hofmann F., Hernanz M., Hartmann D. H., Greiner J., Burwitz V., Fliri J., 2010, A&A, 523, A89
- Henze M., Pietsch W., Haberl F., Hernanz M., Sala G., Hatzidimitriou D., Della Valle M., Rau A., Hartmann D. H., Greiner J., Burwitz V., Fliri J., 2011, A&A, 533, A52
- Hofmann F., Pietsch W., Henze M., Haberl F., Sturm R., Della Valle M., Hartmann D. H., Hatzidimitriou D., 2013, A&A, 555, A65
- Holland S., 1998, AJ, 115, 1916
- Houck J. C., Denicola L. A., 2000, in N. Manset, C. Veillet, & D. Crabtree ed., Astronomical Data Analysis Software and Systems IX Vol. 216 of Astronomical Society of the Pacific Conference Series, ISIS: An Interactive Spectral Interpretation System for High Resolution X-Ray Spectroscopy. p. 591
- Kaaret P., 2002, ApJ, 578, 114
- Kong A. K. H., Garcia M. R., Primini F. A., Murray S. S., Di Stefano R., McClintock J. E., 2002, ApJ, 577, 738
- Maccarone T. J., Yukita M., Hornschemeier A., Lehmer B. D., Antoniou V., Ptak A., Wik D. R., Zezas A., Boyd P., Kennea J., Page K. L., Eracleous

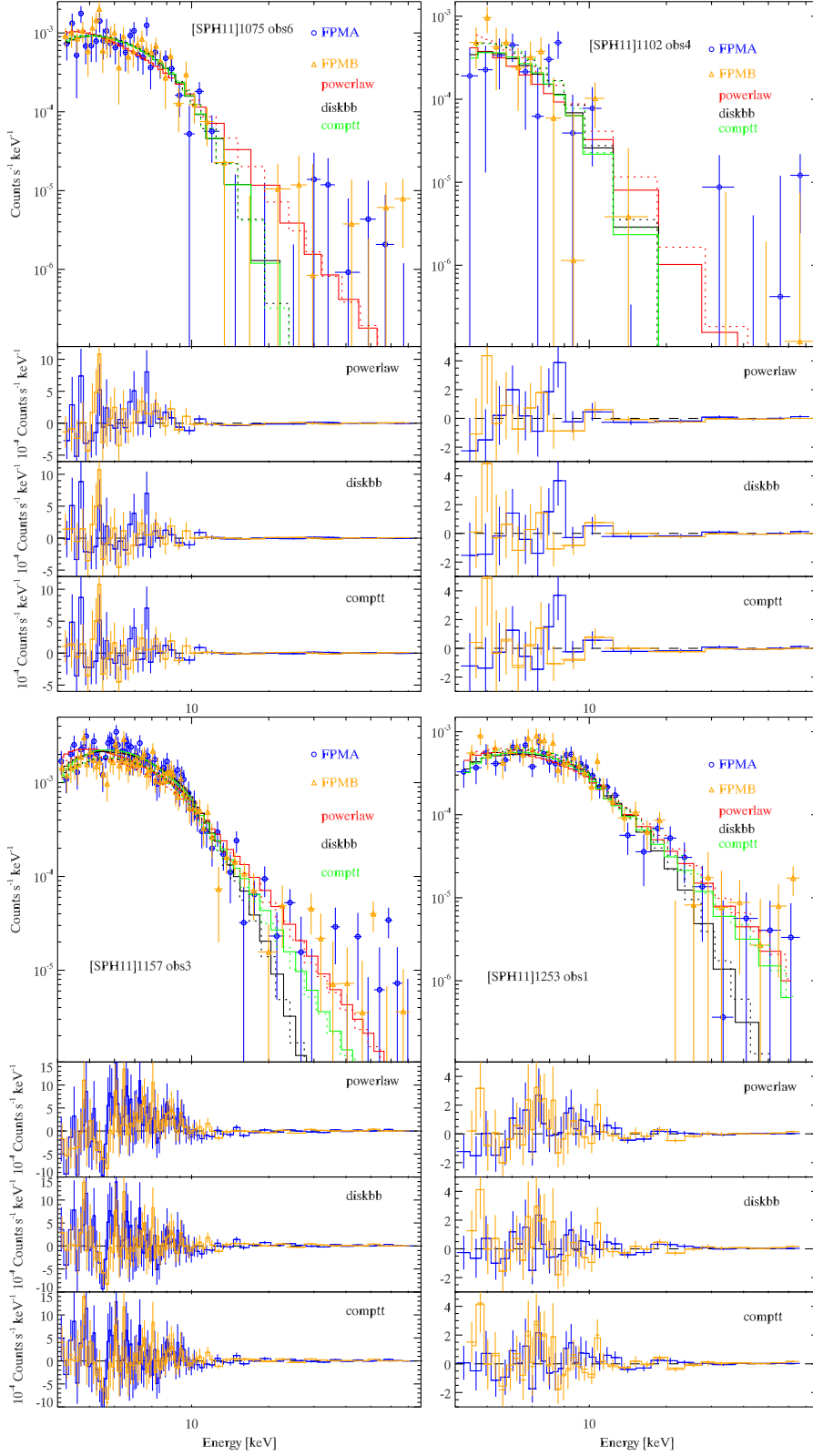


Figure 5. Spectra of [SPH11]1075, 1102, 1157, and 1253. For each source the spectra with the best fit of each model and the residuals for each model are shown.

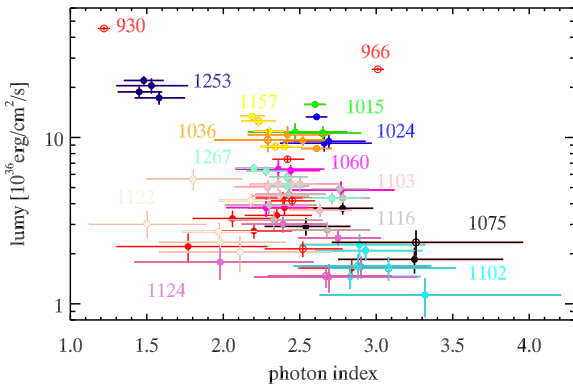


Figure 6. Correlation between photon index and source luminosity.

- M., Williams B. F., Boggs S. E., Christensen F. E., Craig W. W., Hailey C. J., Harrison F. A., Stern D., Zhang W. W., 2016, MNRAS, 458, 3633
 Magnier E. A., 1993, PhD thesis, Massachusetts Institute of Technology
 Marelli M., Tiengo A., De Luca A., Salvetti D., Saronni L., Sidoli L., Paizis A., Salvaterra R., Belfiore A., Israel G., Haberl F., D'Agostino D., 2017, ApJ, 851, L27
 Mitsuda K., Inoue H., Koyama K., Makishima K., Matsuoka M., Ogawara Y., Suzuki K., Tanaka Y., Shibasaki N., Hirano T., 1984, PASJ, 36, 741
 Orio M., Nelson T., Bianchini A., Di Mille F., Harbeck D., 2010, ApJ, 717, 739
 Osborne J. P., Borozdin K. N., Trudolyubov S. P., Priedhorsky W. C., Soaria R., Shirey R., Hayter C., La Palombara N., Mason K., Molendi S., Paerels F., Pietsch W., Read A. M., Tiengo A., Watson M. G., West R. G., 2001, A&A, 378, 800
 Pietsch W., Freyberg M., Haberl F., 2005, A&A, 434, 483
 Pietsch W., Haberl F., 2005, A&A, 430, L45
 Pietsch W., Haberl F., Sala G., Stiele H., Hornoch K., Riffeser A., Fliri J., Bender R., Bühler S., Burwitz V., Greiner J., Seitz S., 2007, A&A, 465, 375
 Primini F. A., Forman W., Jones C., 1993, ApJ, 410, 615
 Rosen S. R., Webb N. A., Watson M. G., Ballet J., Barret D., Braito V., Carrera F. J., Ceballos M. T., Coriat M., Della Ceca R., Denkinson G., Esquej P., Farrell S. A., Freyberg M., Grisé F., Guillout P., Heil L., Koliopanos F., Law-Green D., Lamer G., Lin D., Martino R., Michel L., Motch C., Nebot Gomez-Moran A., Page C. G., Page K., Page M., Pakull M. W., Pye J., Read A., Rodriguez P., Sakano M., Saxton R., Schwonek A., Scott A. E., Sturm R., Traulsen I., Yershov V., Zolotukhin I., 2016, A&A, 590, A1
 Sasaki M., Pietsch W., Haberl F., Hatzidimitriou D., Stiele H., Williams B., Kong A., Kolb U., 2012, A&A, 544, A144
 Shaw Greening L., Barnard R., Kolb U., Tonkin C., Osborne J. P., 2009, A&A, 495, 733
 Shokin Y. A., Kulagina N. B., 1998, Astronomy Letters, 24, 69
 Stanek K. Z., Garnavich P. M., 1998, ApJ, 503, L131
 Stark A. A., Gammie C. F., Wilson R. W., Bally J., Linke R. A., Heiles C., Hurwitz M., 1992, ApJS, 79, 77
 Stiele H., Belloni T. M., Kalemci E., Motta S., 2013, MNRAS, 429, 2655
 Stiele H., Kong A. K. H., 2016, MNRAS, 459, 4038
 Stiele H., Pietsch W., Haberl F., Freyberg M., 2008, A&A, 480, 599
 Stiele H., Pietsch W., Haberl F., Hatzidimitriou D., Barnard R., Williams B. F., Kong A. K. H., Kolb U., 2011, A&A, 534, A55+
 Supper R., Hasinger G., Lewin W. H. G., Magnier E. A., van Paradijs J., Pietsch W., Read A. M., Trümper J., 2001, A&A, 373, 63
 Supper R., Hasinger G., Pietsch W., Truemper J., Jain A., Magnier E. A., Lewin W. H. G., van Paradijs J., 1997, A&A, 317, 328
 Titarchuk L., 1994, ApJ, 434, 570
 Trinchieri G., Fabbiano G., 1991, ApJ, 382, 82
 Trudolyubov S., Priedhorsky W., Cordova F., 2006, ApJ, 645, 277

- Trudolyubov S. P., Borozdin K. N., Priedhorsky W. C., 2001, ApJ, 563, L119
 van Speybroeck L., Epstein A., Forman W., Giacconi R., Jones C., Liller W., Smarr L., 1979, ApJ, 234, L45
 Voss R., Gilfanov M., 2007, A&A, 468, 49
 Voss R., Pietsch W., Haberl F., Stiele H., Greiner J., Sala G., Hartmann D. H., Hatzidimitriou D., 2008, A&A, 489, 707
 Walterbos R. A. M., Brinks E., Shane W. W., 1985, A&AS, 61, 451
 Williams B. F., Garcia M. R., Kong A. K. H., Primini F. A., King A. R., Di Stefano R., Murray S. S., 2004, ApJ, 609, 735
 Williams B. F., Garcia M. R., McClintock J. E., Primini F. A., Murray S. S., 2006, ApJ, 637, 479
 Williams B. F., Naik S., Garcia M. R., Callanan P. J., 2006, ApJ, 643, 356
 Wilms J., Allen A., McCray R., 2000, ApJ, 542, 914
 Yukita M., Ptak A., Hornschemeier A. E., Wik D., Maccarone T. J., Pottschmidt K., Zezas A., Antoniou V., Ballhausen R., Lehmer B. D., Lien A., Williams B., Baganoff F., Boyd P. T., Enoto T., Kennea J., Page K. L., Choi Y., 2017, ApJ, 838, 47

This paper has been typeset from a TeX/LaTeX file prepared by the author.

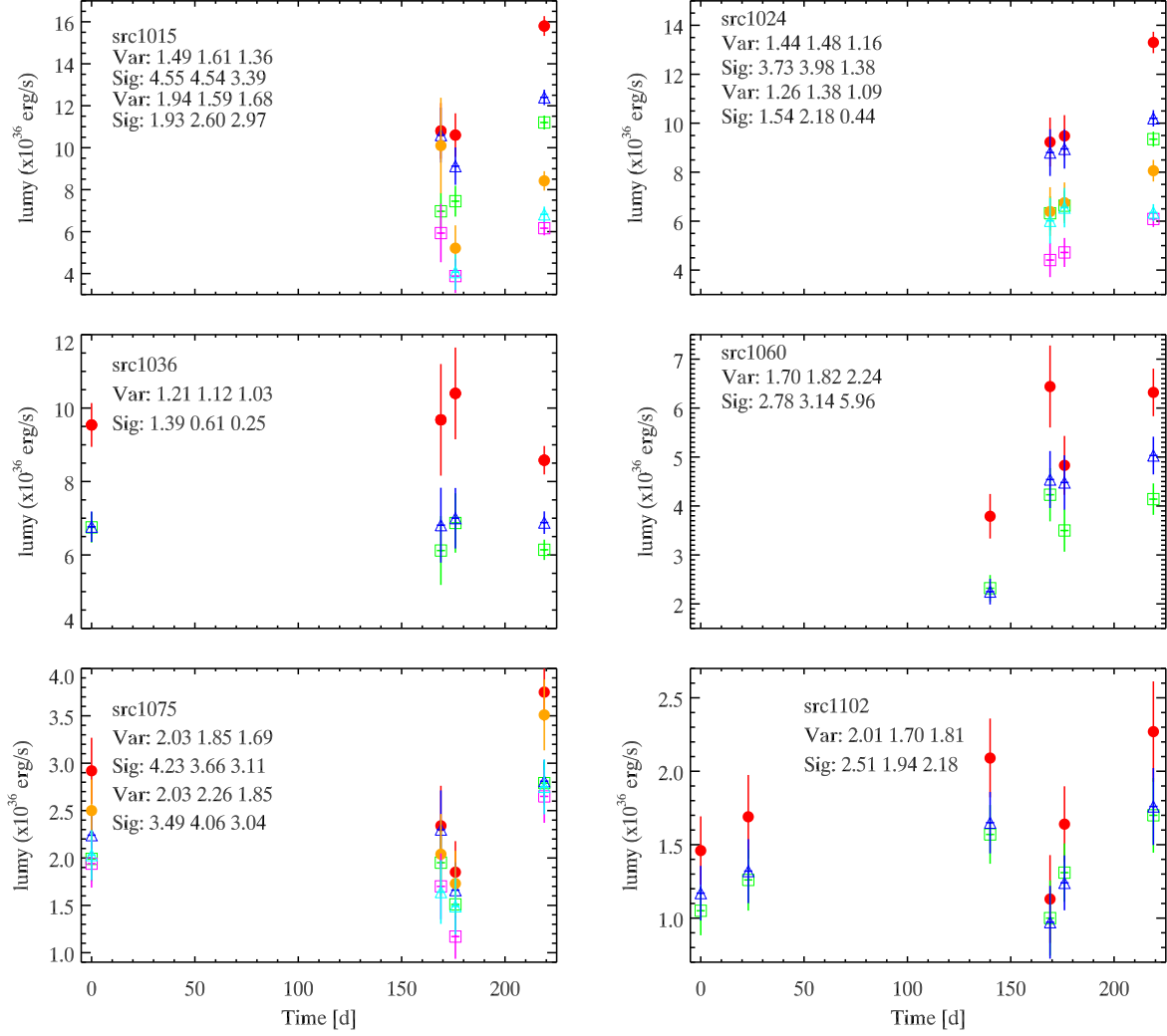
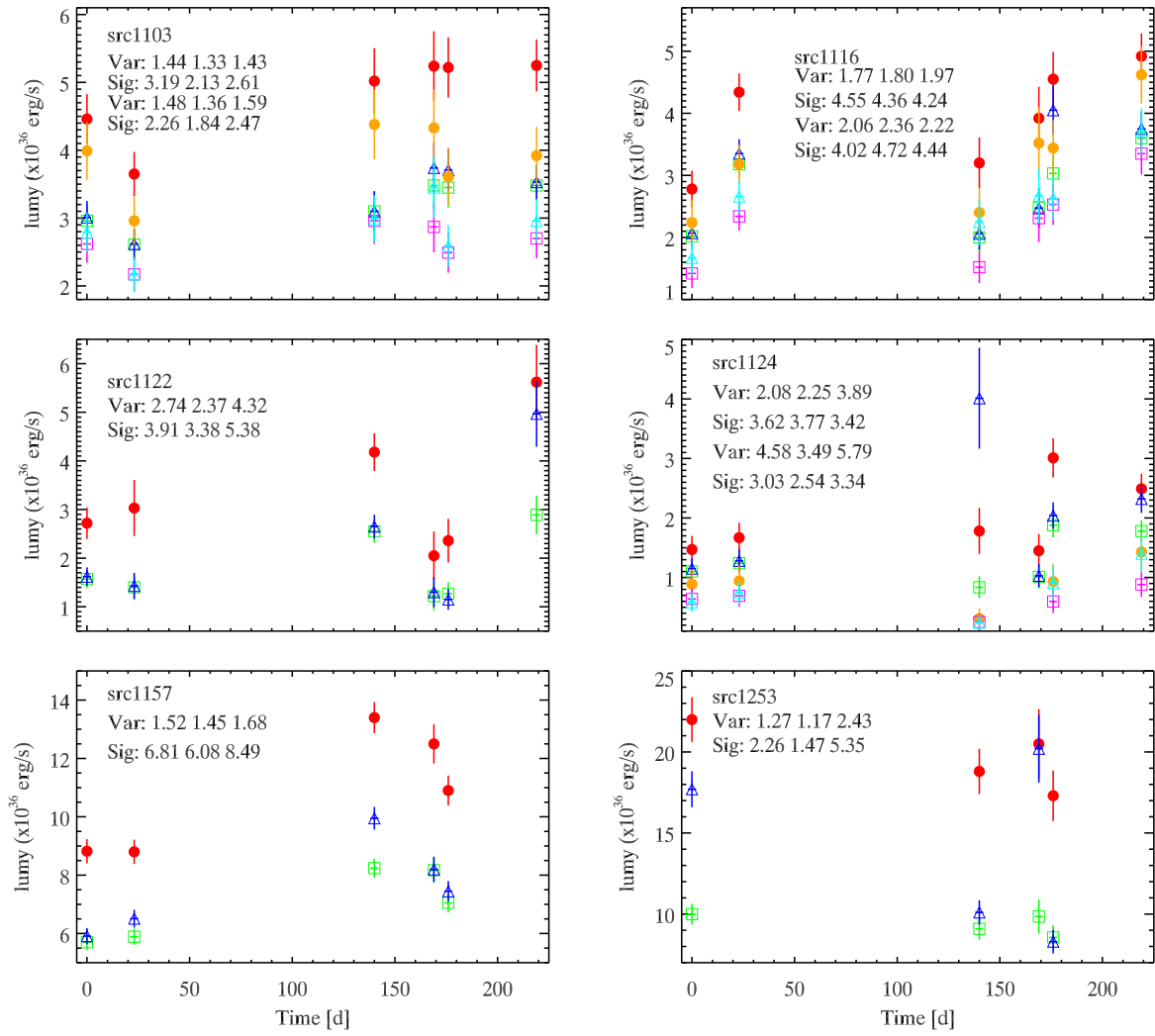
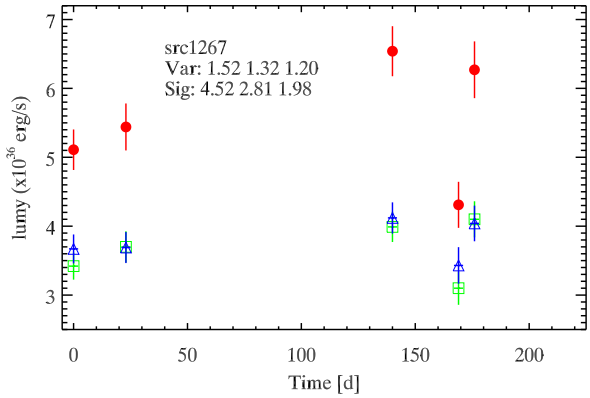
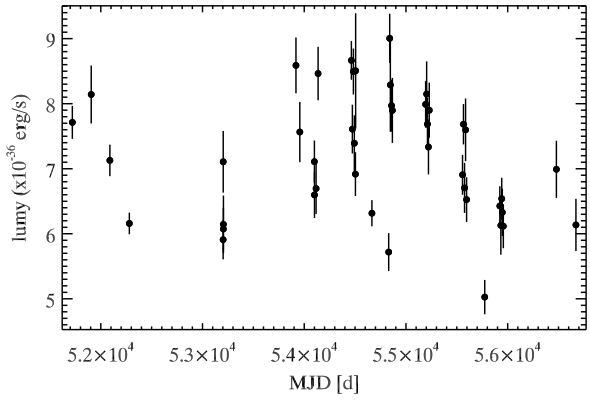


Figure 7. Long term light curves of the 13 sources that were observed more than once, derived from the fits of the energy spectra. Luminosities obtained from the power law fit are given as red filled dots, those from the disk blackbody fit as green open squares, and those from the Comptonization model as blue open triangles. The ratio of the maximum and minimum luminosity (Var) and the significance of the luminosity difference (Sig) are given for each spectral model (power law, disk blackbody, Comptonization model). For [SPH11] 1015, 1024, 1075, 1103, 1116, and 1124 we also show luminosities derived from extraction regions of $15''$ (power law: orange dots; disc blackbody: magenta squares; Comptonization model: cyan triangles).

**Figure 7.** continued

**Figure 7.** continued**Figure 8.** Long term *XMM-Newton* light curve of [SPH11] 1253.